Dielectric and ferroelectric properties of $(Bi_{0.5}Na_{0.5})_{0.94}Ba_{0.06}Ti_{1-x}Al_xO_{3-\delta}$ lead-free ferroelectric ceramics

Han-li Lian[1] · Rui-xue Cheng[1] · Yan-zi Qiu[2] · Jin-yan Shi[1] · Xiao-ming Chen[2]

Abstract

Microstructure and dielectric properties of the lead-free ferroelectric ceramics $(Bi_{0.5}Na_{0.5})_{0.94}Ba_{0.06}Ti_{1-x}Al_xO_{3-\delta}$ (abbreviated as BNBTA/x, $x = 0$, 0.04, 0.06, 0.08) obtained via a solid-state reaction method were studied. The ceramics with x≤0.06 exhibit pure structure without detectable secondary phase by X-ray diffraction measurement. There appears a second phase in the ceramic BNBTA/0.08. With an increase in the Al^{3+} amount, dielectric constant of the ceramics decreases, and the change in dielectric constant with increasing temperature between the two dielectric characteristic temperatures (T_{RE} and T_m) is gradual. The poled ceramic BNBTA/0 shows a steep increase in permittivity at the temperature denoted as T_d around 100 °C. But, the poled ceramics with $x > 0$ do not exhibit the T_d anomaly on the permittivity spectra. The diffuse dielectric behavior around T_m was studied via the Curie–Weiss law and modified Curie–Weiss law. Compared to the ceramic BNBTA/0, the Al^{3+} -doped ceramics show slim ferroelectric hysteresis loops. The temperature-dependent ferroelectric properties and energy-storage behavior were studied.

1 Introduction

$Bi_{0.5}Na_{0.5}TiO_3$ (BNT) is considered to be a good lead-free ferroelectric material with excellent ferroelectric properties at room temperature. However, pure BNT has poor dielectric performance and is difficult to be polarized [1]. In order to improve dielectric performance, a serial of BNT-based solids have been extensively investigated, such as BNT-BaTiO3 [2–4], BNT-Bi0.5K0.5TiO3 [5], $(Na_{0.5}Bi_{0.5})_{0.4}Sr_{0.6}Ti_{1-x}Sn_xO_3$ [6], 0.93BNT-0.07BaTiO3-BiAlO3 [7], 0.94BNT-0.06BaTi1−xZrxO3 [8], etc. Zhu et al. reported that NaNbO3-doped 0.95Bi0.5Na0.5TiO3-0.05SrZrO3 exhibited the coexistence of rhombohedral and tetragonal phases and the variation in the dielectric permittivity can be less than ±15% over the temperature range from −55 to 545 °C [9]. McLaughlin et al. found that $(Bi_{0.4-x/3}Na_{0.4-x/3}Sr_{0.2-x/3}Er_x)TiO_3$ with $x = 0.015$ showed

enhanced thermal stability of the maximum achievable electric field induced strain over the 25–175 °C temperature range [10]. Among the BNT -based ceramics, the composition $(Bi_{0.5}Na_{0.5})_{0.94}Ba_{0.06}TiO_3$ (denoted as BNBT) exhibits excellent dielectric and ferroelectric properties [11, 12]. Various elements have been doped into BNBT. Liu et al. reported the enhanced electrical and photoluminescence properties of the Er^{3+} -doped BNBT ceramics [13]. Jing et al. found that the radii of doping cations at the A-site play key role in affecting structure, dielectric, and piezoelectric properties of the BNBT -based ceramics [14]. Li et al. observed that the doping of BaSnO3 in BNBT -based ceramics enhanced the breakdown strength of the ceramics and improved energy-storage properties [15]. Fan and Tan explored the correlation between the polarization degradation and the phase transition reversibility in (1-x) $Bi_{0.5}Na_{0.5}TiO_3$-xSrTiO3 ceramics via in-situ transmission electron microscopy fatigue tests [16]. Zhang et al. reported the enhanced energy-storage performance in Sn-doped $Sr_{0.6}(Na_{0.5}Bi_{0.5})_{0.4}TiO_3$ lead-free relaxor ferroelectric ceramics [17]. Previously, we reported that the doping of Ca^{2+} can improve ferroelectric behavior and increase depolarization temperature of BNBT -based ceramics [18], while the doping of Sr^{2+} can improve stability of piezoelectric constant (d_{33}) at elevate temperatures [19]. The ions of transition elements, such as Fe^{3+} [20, 21], Co^{3+} [22], Ni^{2+} [23], etc.,

✉ Han-li Lian
lianhanli@163.com

1 School of Science, Xi'an University of Posts and Telecommunications, 710121 Xi'an, People's Republic of China

2 School of Physics and Information Technology, Shaanxi Normal University, 710119 Xi'an, People's Republic of China

have also been doped into BNBT to tune their dielectric and ferroelectric behavior, in which oxygen vacancies are very important in influencing their dielectric and ferroelectric properties. All these results demonstrate that doping cations can effectively influence dielectric and piezoelectric properties of BNT -based ceramics.

Doping of Al^{3+} can result in large polarization in the resulting materials [24]. Al^{3+} ions have been doped into various materials, such as $PbTiO_3$ [25], $PbZrO_3$ [26], and $BaTiO_3$ [27], and so on. Yu et al. reported that the $(1-x)(Na_{0.5}Bi_{0.5})TiO_3$-$xBiAlO_3$ ceramics show significantly reduced dielectric loss [28]. Ullah et al. explored temperature-insensitive large strain in $BiAlO_3$-modified $Bi_{0.5}(Na_{0.75}K_{0.25})_{0.5}TiO_3$ ceramics [29]. Fu et al. pointed out that the doping of $BiAlO_3$ into $Bi_{0.5}(Na_{0.82}K_{0.18})_{0.5}TiO_3$ can improve electrical properties of the ceramics [30]. Qiu et al. reported the key role of polarization in affecting lattice distortion and strain for the $0.97(Bi_{0.5}Na_{0.5})_{0.94}Ba_{0.06}TiO_3$-$0.03BiAlO_3$ ceramics [31]. Wang et al. studied the effects of $BiAlO_3$ doping content on microstructure and dielectric properties of the $(1-x)(0.93Bi_{0.5}Na_{0.5}TiO_3$-$0.07BaTiO_3)$-$xBiAlO_3$ ceramics and found that the ceramics with $x=0.01$ have increased Curie temperature, piezoelectric, and ferroelectric properties [7]. The studies show that $BiAlO_3$ can significantly change electrical behavior of BNBT -based ceramics. The radius (r) of Al^{3+} is 0.0535 nm in the case of coordination number CN = 6, which is comparative with that of Ti^{4+} ($r=0.0605$ nm with CN = 6) [32]. Al^{3+} can enter into the Ti^{4+} site. In addition, the doping of Al^{3+} will cause oxygen vacancies in the ceramics because of the lower electric charge of Al^{3+} than that of Ti^{4+}. Here, we report the preparation of $(Bi_{0.5}Na_{0.5})_{0.94}Ba_{0.06}Ti_{1-x}Al_xO_{3-\delta}$ lead-free ferroelectric ceramics and characterization of their dielectric properties.

2 Experimental procedure

Lead-free ceramics $(Bi_{0.5}Na_{0.5})_{0.94}Ba_{0.06}Ti_{1-x}Al_xO_3$ (BNBTA/x, $x=0$, 0.04, 0.06, 0.08) were prepared via a solid-state reaction method. $BaCO_3$ ($\geq 99.0\%$), TiO_2 ($\geq 98.0\%$), Na_2CO_3 ($\geq 99.8\%$), Bi_2O_3 ($\geq 98.9\%$), and Al_2O_3 ($\geq 99.99\%$) powders were used as starting materials. The raw powders were placed in an oven at 120 °C for 24 h for drying and then weighed according to the chemical ratio. The powders were ball-milled in a planetary mill for 24 h and then calcined at 900 °C for 3 h. After calcination, the powders were ball-milled again for 8 h. The binder of 5% PVA was added into the powders. Disk-shaped green pellets with diameter 10 mm and thickness 1.2 mm were pressed. Then, the binder was burned out at 500 °C for 2 h. The green pellets were sintered at 1170 °C for 3 h at the heating rate of 3 °C/min. During sintering, the pellets were buried using the powders

with the same composition to reduce the volatilization of elements Bi and Na.

Phase structure of the samples was analyzed via a X-ray diffractometer of Rigaku D/MAX2550. Morphology of the ceramics was observed using a scanning electronic microscope (SEM, Nova Nano 450). For SEM measurement, the ceramics were mechanically polished and then thermally etched at 900 °C for 1 h. The samples were poled in silicone oil at 5 kV/mm for 0.5 h. The temperature-dependent dielectric spectra of the poled ceramics were measured via a LCR meter (Agilent E4980A, Santa Rosa, CA). Ferroelectric performance was characterized using a RADIANT ferroelectric testing system (Precision Premier II, Radiant Technologies Inc. Albuquerque, NM).

3 Results and discussion

Figure 1 shows the XRD curves of the samples. The samples with $x=0$, 0.04, and 0.06 display pure perovskite structure with pseudo-cubic phase. However, the sample with $x=0.08$ shows a second phase, suggesting that the doping amount of Al^{3+} with $x=0.08$ exceeds the solid solution limit. The similar phenomenon was also found in the $BiAlO_3$-modified $Bi_{0.5}Na_{0.5}TiO_3$-$Bi_{0.5}K_{0.5}TiO_3$ ceramics, in which the secondary phase was identified as $Na_{0.5}Bi_{4.5}Ti_4O_{15}$ indexed according to JCPDS No. 74-1316 [33]. An enlarged view of the XRD peak around 32° is shown in Fig. 1(b). For the ceramics with $x \leq 0.06$, the peak position shifts towards a high-angle direction with increasing x, indicating shrinkage of the unit cell caused by the Al^{3+} doping. As mentioned above, the radii of Al^{3+} and Ti^{4+} with coordination number (CN) of 6 are 0.535 Å and 0.605 Å, respectively [32]. The substitution of Al^{3+} for the Ti^{4+} results in contraction of the unit
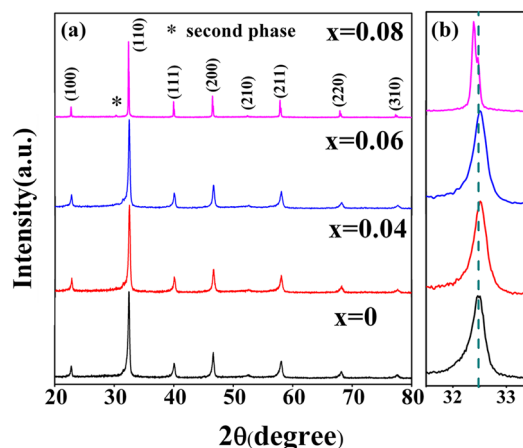

Fig. 1 X-ray diffraction patterns of the BNTBA/x ceramics (**a**). The peaks were indexed according to JCPDS No. 89-3109. The enlarged region at 2θ ranges from 31.5° to 33.5° (**b**)

cell because of smaller size of Al^{3+}. In addition, the doping of Al^{3+} will introduce oxygen vacancies in the ceramics (as demonstrated in Eq. (1) via the Kröger–Vink formula), which should also contribute to distortion of the unit cell.

$$Al_2O_3 \rightarrow V_O^{\bullet\bullet} + 2Al_{Ti}' + 2O_O^{\times} + 1/2O_2(g) \tag{1}$$
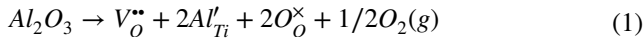
For the ceramic with $x = 0.08$, the diffraction peak shifts to a low-angle direction, which may be related to the secondary phase.

Figure 2 displays top-view SEM images of the thermally etched surfaces of the samples of different doping levels. All the ceramics exhibit dense microstructures. The grain size distribution was calculated via more than 200 grains in each sample and is shown in the insets of Fig. 2. The average grain sizes for the samples with $x = 0$, 0.04, 0.06, and 0.08 are 1.2±0.9 μm, 0.8±0.5 μm, 0.8± 0.5 μm, and 0.6±0.3 μm, respectively. Grain sizes decrease slightly with the doping of Al^{3+}. For the ceramic with $x = 0.08$, needle-like secondary phase was observed, which is consistent with the XRD result.

The temperature-dependent dielectric spectra of the poled ceramics are illustrated in Fig. 3. For the ceramic without

Al^{3+} doping, three dielectric anomalies are observed on the curves of dielectric constant (ε_r) with increasing temperature at the given temperatures, which are denoted as T_d, T_{RE}, and T_m. T_d corresponds to the temperature at which a peak appears on the dielectric loss ~ temperature curves. At temperatures lower than T_d, dielectric constant at different frequencies merges together. T_d is usually used to determine depolarization temperature, below which the ferroelectric state is stable [34]. As temperature is increased up to T_d, the long-range ordered ferroelectric state is broken [34–36]. The T_d value for the sample with $x = 0$ is about 100 °C. But, the dielectric anomaly around T_d disappears for the Al^{3+}-doped ceramics, implying that depolarization temperature decreases below room temperature, as reported by others [7, 31]. All the samples show the characterization temperatures T_{RE} and T_m. T_{RE} corresponds to the temperature at which the difference of dielectric constant at different frequencies ($\Delta\varepsilon_r = \varepsilon_{r,1kHz} - \varepsilon_{r,100kHz}$) becomes minimum (Fig. 3), where $\varepsilon_{r,1kHz}$ and $\varepsilon_{r,100kHz}$ are dielectric constant at 1 kHz and 100 kHz, respectively. Below T_{RE}, dielectric constant has a strong dependence on frequency, corresponding to ergodic relaxor behavior [37]. As temperature increases up to T_{RE}, dielectric permittivity at different frequencies tend to merge
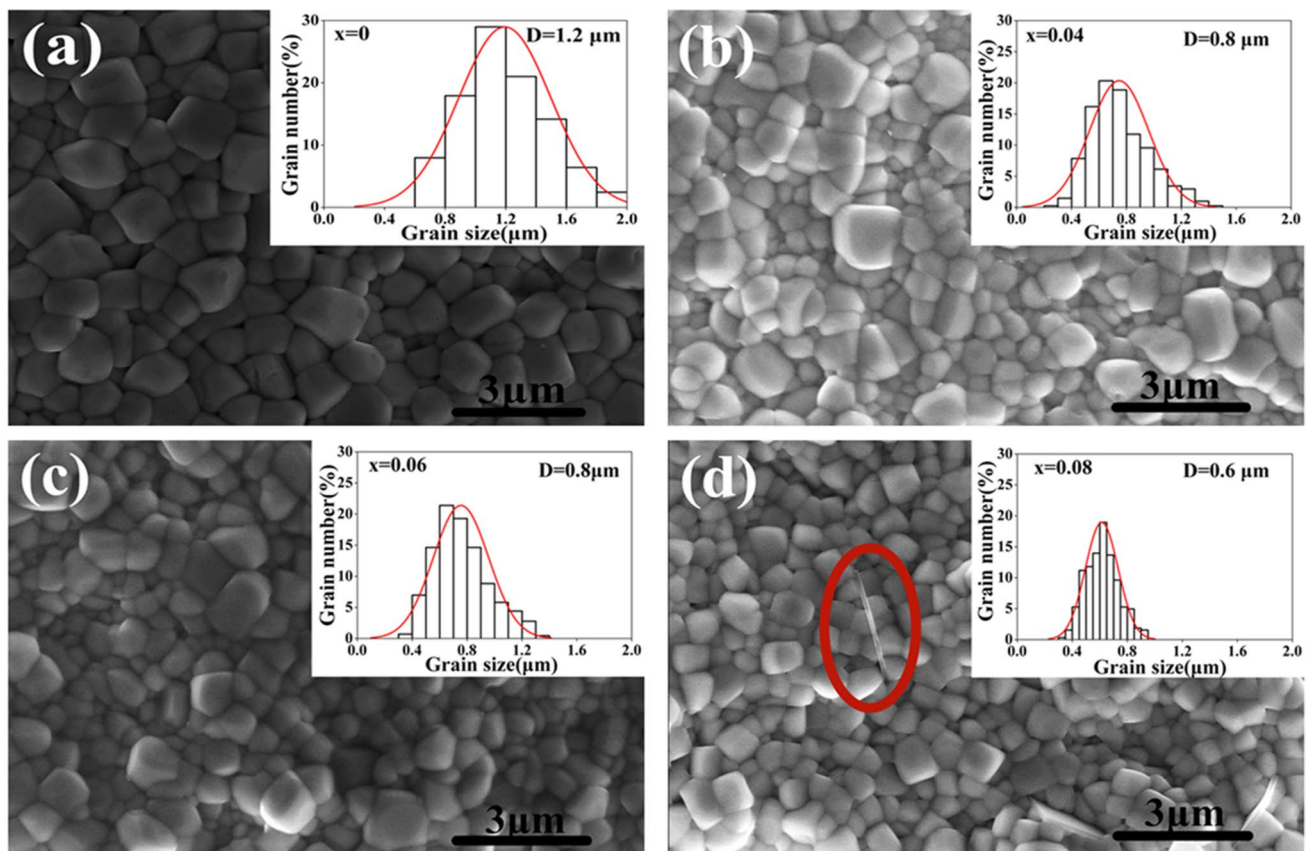

Fig. 2 SEM micrographs of the surfaces of the BNTBA/x ceramics with $x = 0$ (**a**), $x = 0.04$ (**b**), $x = 0.06$ (**c**) and $x = 0.08$ (**d**)
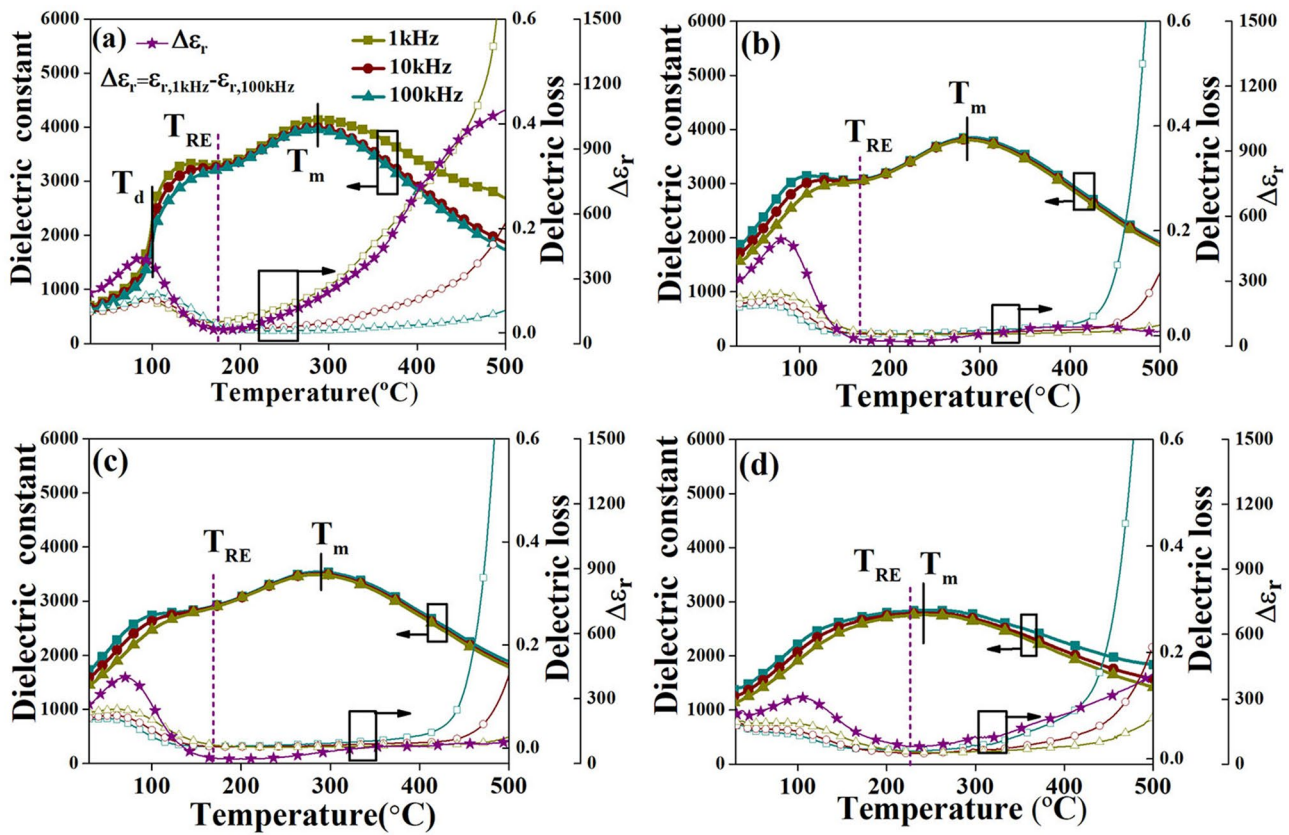
Fig. 3 Dielectric constant and dielectric loss vs. temperature for the poled BNTBA/x ceramics with x=0 (a), x=0.04 (b), x=0.06 (c), and x=0.08 (d). The values of $\Delta\varepsilon_r = \varepsilon_{r},1\text{kHz} - \varepsilon_{r},100\text{kHz}$ are also shown

together. T_m corresponds to the temperature at which dielectric constant increases to a maximum (ε_m). The T_m is also reported as Curie point for BNT-based ceramics [38]. It is suggested that the dielectric anomalies around T_{RE} and T_m are associated with evolution of polar nanoregions (PNRs) as temperature changes [39]. The ceramics with $x=0$, 0.04, 0.06, and 0.08 have T_{RE} values 174 °C, 169 °C, 170 °C, and 225 °C, respectively. The corresponding T_m values are 283 °C, 286 °C, 287 °C, and 244 °C, respectively. As can be seen from the dielectric spectra, the Al^{3+} doping causes a decrease in dielectric permittivity. In order to detect the difference of dielectric constant at T_{RE} and T_m, the values of $\Delta\varepsilon_r' = \varepsilon_m - \varepsilon_{RE}$ were determined. The ε_m values at T_m for the samples with $x=0$, 0.04, 0.06, and 0.08 are 4138, 3853, 3541, 2844, respectively. The corresponding permittivity values at T_{RE} (ε_{RE}) are 3352, 3080, 2923, 2802, respectively. The values of $\Delta\varepsilon_r'$ for the samples with $x=0$, 0.04, 0.06, and 0.08 are 807, 470, 487, and 11, respectively. The Al^{3+} -doping causes decrease in $\Delta\varepsilon_r'$ during the temperature window $\Delta T = T_m - T_{RE}$ of 98 °C, 114 °C, 119 °C, and 43 °C for the samples with $x=0$, 0.04, 0.06, and 0.08, respectively. By doping Al^{3+}, the ceramics exhibit better frequency stability and temperature stability of dielectric constant at

temperatures between T_{RE} and T_m. Broad T_m peaks on the $\varepsilon_r \sim T$ curves indicate diffuse phase transition behavior. The diffuse phase transition behavior was studied according to the Curie–Weiss law: (Eq.2)

$$1/\varepsilon_r = (T - T_0)/C \tag{2}$$

where T_0 is defined as the Curie–Weiss temperature, and C is a constant. The fitting results of $1/\varepsilon_r$ as a function of temperature T at 10 kHz for all the samples are shown in Fig. 4. At the temperatures denoted as T_B (i.e., Burns temperature), the change of $1/\varepsilon_r$ as a function of T deviates from the Curie–Weiss law with decreasing temperature. The T_B values for the samples with $x=0$, 0.04, 0.06, and 0.08 are 413 °C, 439 °C, 445 °C, 385 °C, respectively. As x≤0.06, the T_B values increase with the increase in the Al^{3+} content. The doping of Al^{3+} introduces oxygen vacancies. As the doping content increases, oxygen vacancy concentration increases and improves the stability of polar nanodomains [31]. So, the T_B values increase. But, the sample with $x=0.08$ exhibits decreased T_B value. The related mechanism is still unclear, which may be related to the appearance of the second phase. The relationship between dielectric constant and temperature

Fig. 4 The relationship between $1/\varepsilon_r$ and temperature at 10 kHz for the BNTBA/x ceramics with x = 0 (a), x = 0.04 (b), x = 0.06 (c), and x = 0.08 (d). The solid lines are fitting results via the Curie–Weiss law
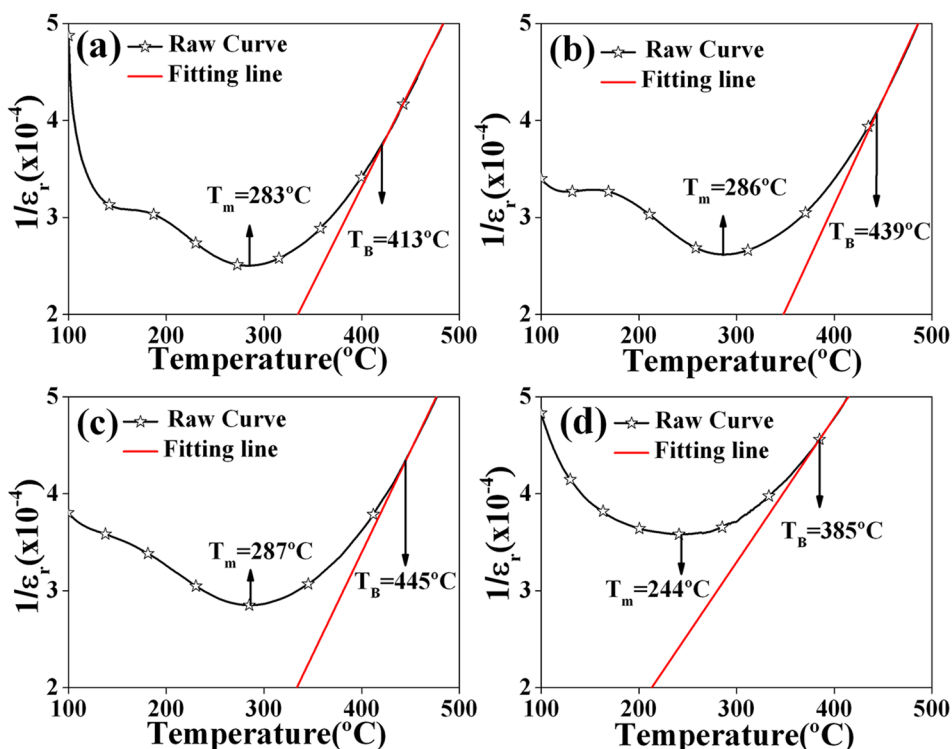
was further studied by means of the modified Curie–Weiss law, which is as follows: (Eq.3)

$$1/\varepsilon_r - 1/\varepsilon_m = (T - T_c)^\gamma / C',$$ (3)

where C′ is a Curie-like constant and γ is defined as diffusion coefficient. The γ value of a normal ferroelectric is 1, while a relaxor ferroelectric has $\gamma = 2$ [40]. The fitting results via the modified Curie–Weiss equation are exhibited in Fig. 5. The γ values of the samples with x = 0, 0.04, 0, 06, and 0.08 are 1.79, 1.92, 1.94, and 1.91, respectively, suggesting obvious dielectric diffuseness behavior. The doped ceramics exhibit increased γ values compared to the sample with x = 0. The diffuse phase transition character in BNT-based ceramics is always suggested to be closely associated with the coexistence of Bi^{3+}, Na^+, and Ba^{2+} at the A-sites, as well as Ti^{4+} and the dopants at the B-site [7]. So, the increase of γ value is related to the increase of Al^{3+} doping amount and oxygen vacancy content.

Figure 6 shows the curves of polarization (P) as a function of measurement electric field (E). The sample with x = 0 exhibits typical ferroelectric P-E loops. With the increase in E, the P-E loops tend to be saturated. The current density (J) as a function of electric field at E = 70 kV/cm is also given. Two typical peaks exist on the J-E curve, corresponding to domain switching with changing electric field [41]. All the Al^{3+}-doped ceramics exhibit constricted P-E loops. Even under the maximum electric field of 70 kV/cm, the samples still show slim P-E loops. With the increase in the amount of Al^{3+} from x = 0.04 to x = 0.08, the P-E loops become slimmer. The ceramic with x = 0.04 exhibits four current peaks on the J-E curve, which are denoted as $\pm E_F$ and $\pm E_R$ in the different quadrants (Fig. 6b). It has been suggested that the emergence of the peaks around $\pm E_F$ and $\pm E_R$ are related to the coexistence of ergodic and non-ergodic phases [42]. As the Al^{3+} content further increases to x = 0.06 and 0.08, the peaks on the J-E curves become increasingly blurred / disappeared, which are typical character for relaxor ferroelectrics [43, 44]. The values of coercive field (E_c), remnant polarization (P_r), and maximum polarization (P_m) are shown in Fig. 7 (a-c). With an increase in electric field, the E_c, P_m, and P_r values increase. The values of E_c, P_r, and P_m of the samples under E = 70 kV/cm are compared in Fig. 7(d). The sample with x = 0 has the largest E_c, P_r, and P_m values due to its typical ferroelectric behavior. As the Al^{3+} amount increases, both the values of polarization and E_c decrease because of their slimmer P-E loops. The doping of Al^{3+} disrupts long-range-ordered ferroelectric phase and results in a sharp decline in the polarization and E_c values. The Al^{3+}-doped ceramics exhibit ergodic relaxor behavior, which is characterized by the constriction of P-E loops with small polarization and coercive field. The results are in accordance to the dielectric permittivity spectra (Fig. 3b-d). The constricted P-E loops help to improve energy-storage properties of materials. Discharge energy density (W_1) can be calculated by integrating the area between the polarization

Fig. 5 The fitting results according to the modified Curie–Weiss law at 1 kHz for the BNTBA/x ceramics with $x=0$ (a), $x=0.04$ (b), $x=0.06$ (c), and $x=0.08$ (d)
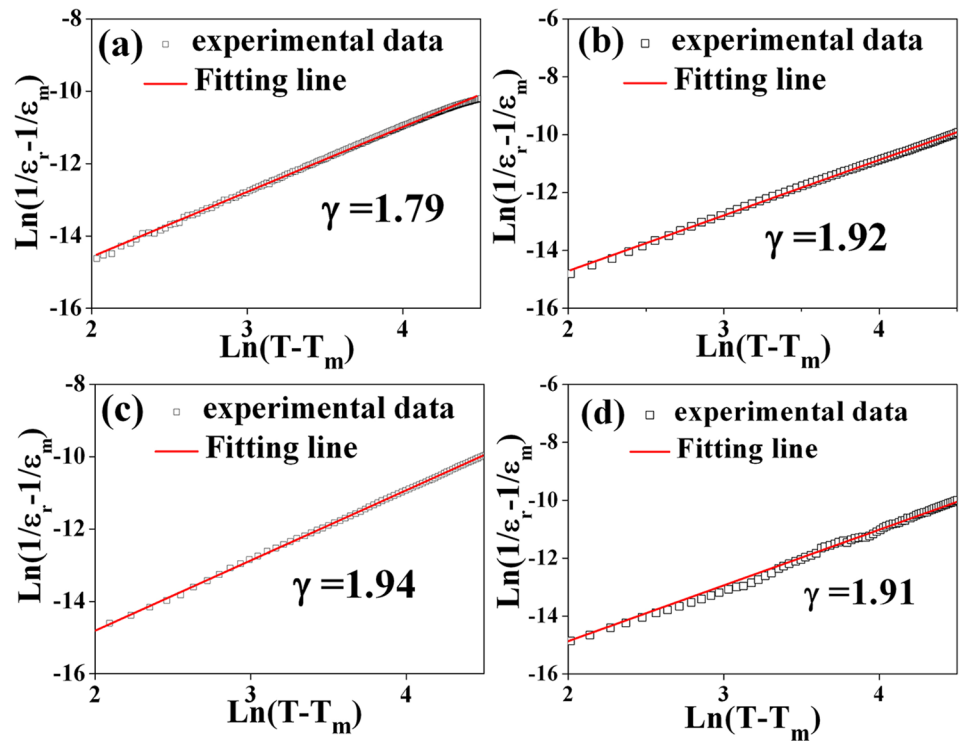
axis and the discharge curve of the P-E hysteresis loops via Eq. (4):

$$W_1 = \oint_{P_r}^{P_m} E dp. \tag{4}$$

The energy-storage efficiency (η) values can be calculated via Eq. (5):

$$\eta = W_1 / \left(W_1 + W_{loss} \right) \times 100\%, \tag{5}$$

in which W_{loss} is obtained by integrating the area between the charge and discharge curves. The W_1 and η values for the present samples under the maximum measurement electric field 70 kV/cm at room temperature are presented in Table 1. The ceramic with $x=0.06$ exhibits the largest W_1 of 0.82 J/cm^3 and relatively high $\eta=67.7\%$ at room temperature under $E=70$ kV/cm. The typical samples with $x=0$ and $x=0.06$ were chosen to study temperature-dependent ferroelectric and energy-storage properties. The temperature-dependent hysteresis loops of the ceramics with x = 0 and x = 0.06 measured at $E=50$ kV/cm are shown in Fig. 8(a,b). For the ceramic with $x=0$, the P-E loops become slimmer with the increase in the measurement temperatures. Around 100 °C, the polarization decreases obviously (Fig. 8c). It corresponds to the characteristic temperature T_d via the dielectric spectra (Fig. 3). The dramatically changes in the P-E loops of the $x=0$ sample with increasing temperature should be attributed to the thermal-induced weakened

ferroelectricity and the appearance of an ergodic relaxor phase. For the sample with $x=0.06$, the P-E loops change little with the increase in the measurement temperature. As has been demonstrated in the dielectric spectra of the sample with $x=0.06$ (Fig. 3c), the ergodic relaxor behavior always exists as temperature increases up to T_{RE}. During the measurement temperature range, the sample with $x=0.06$ shows slight change in the P-E loops. Compared to remarkable change in polarization of the sample with $x=0$, the sample with $x=0.06$ exhibits gentle variation of polarization with increasing temperature, demonstrating good temperature stability (Fig. 8d). The calculated W_1 and η values of the both samples at the different measurement temperatures are shown in Fig. 8(e,f). For the ceramic with $x=0$ under the measurement electric field $E=50$ kV/cm, as the measurement temperature increases from room temperature to 180 °C, the W_1 and η values change from 0.15 J/cm^3 and 10.6% to 0.41 J/cm^3 and 65.2%, respectively. For the ceramic with $x=0.06$, the corresponding values of W_1 and η at room temperature are 0.78 J/cm^3 and 71.3%, respectively; and those at 180 °C are 0.76 J/cm^3 and 84.5%, respectively (Table 1). The energy-storage properties of the BNT-based ceramics reported by others are also compared in Table 1[1]. Li et al. reported that the ceramic 0.97BNBT-0.03CaZrO$_3$ showed the W_1 value of approximate 0.63 J/cm^3 under $E=60$ kV/cm at 130 °C [45]. Yin et al. prepared the ceramics $\{\{Bi_{0.5}[(Na_{0.8}K_{0.2})_{0.9}Li_{0.1}]_{0.5}\}\}_{0.96}$-Sr$_{0.04}$(Ti$_{0.975}Ta_{0.025}$)O$_3$ via the hot-pressed sintering method and reported their
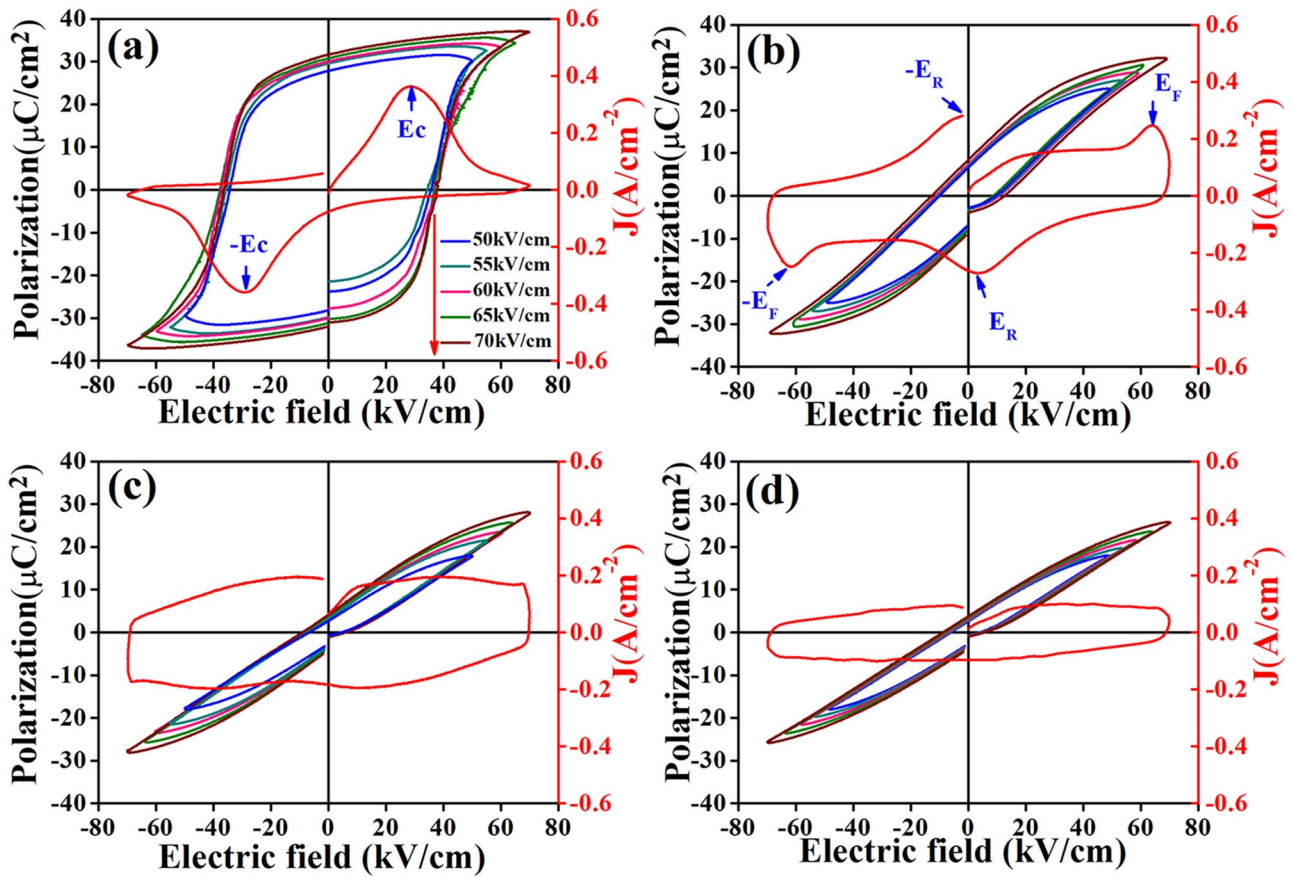
Fig. 6 The P-E loops measured at electric fields between 50 and 70 kV/cm, and J-E loops measured at 70 kV/cm for the BNTBA/x ceramics with $x=0$ (**a**), $x=0.04$ (**b**), $x=0.06$ (**c**), and $x=0.08$ (**d**). The measurement frequency is 20 Hz

Fig. 7 The values of P_m (**a**), P_r (**b**), and E_c (**c**) for the BNTBA/x ceramics measured under the different electric fields. The values of P_m, P_r, and E_c measured at 70 kV/cm as a function of x
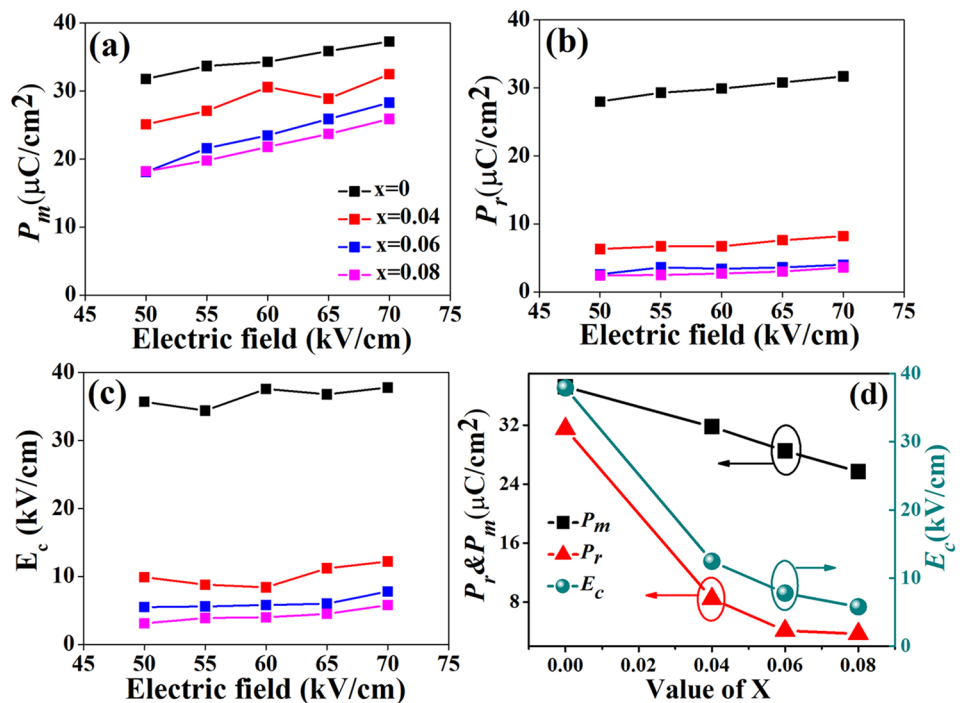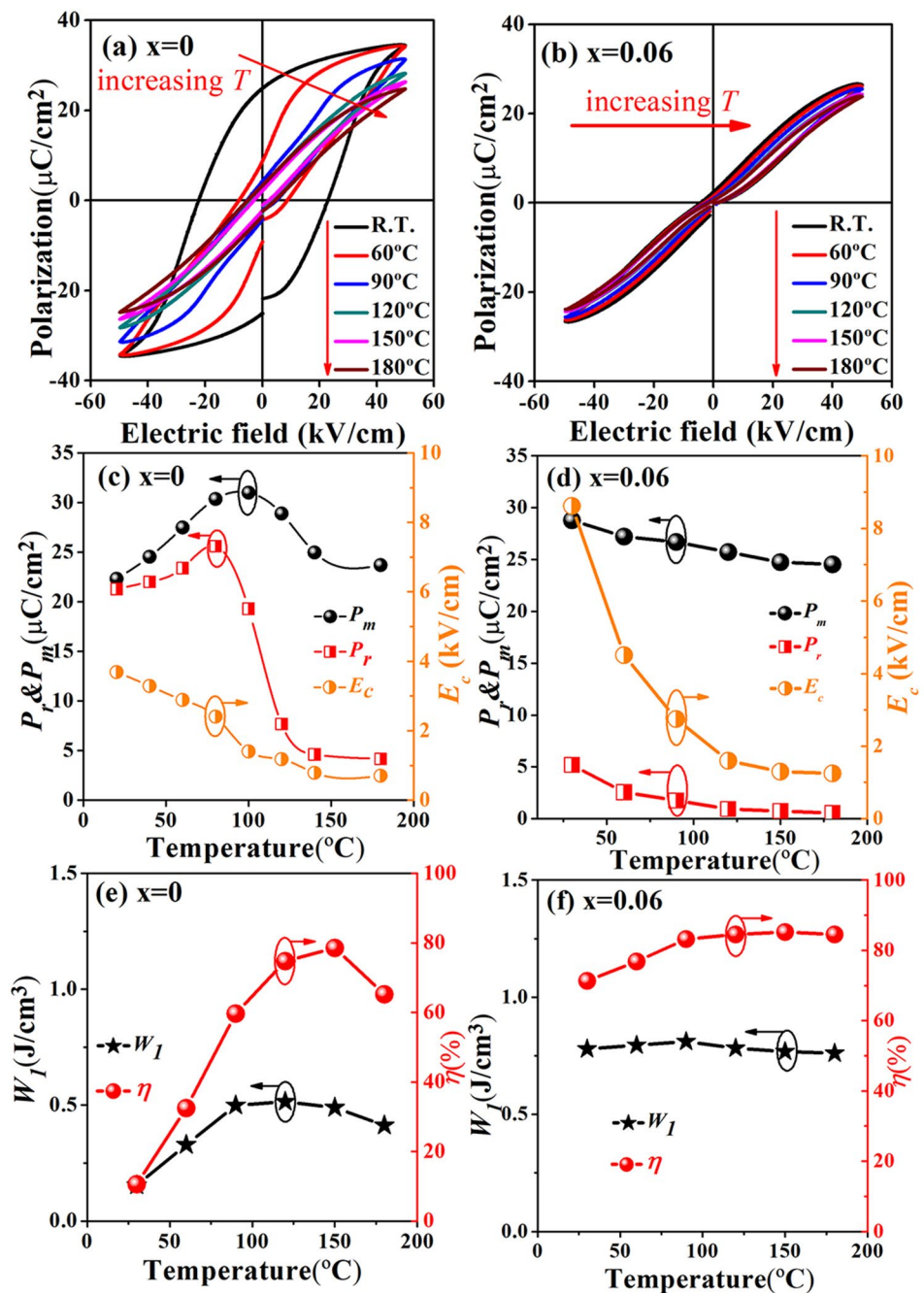
Fig. 8 The P-E loops measured under the electric field 50 kV/cm at the different temperatures for the samples with $x = 0$ (**a**) and $x = 0.06$ (**b**). The values of P_m, P_r, and E_c at the different temperatures for the samples with $x = 0$ (**c**) and $x = 0.06$ (**d**). The values of W_1 and η at the different temperatures for the samples with $x = 0$ (**e**) and $x = 0.06$ (**f**)

excellent discharge energy density $W_1 > 2$ J/cm^3 between room temperature and 175 °C under E = 130 kV/cm [46]. Zhang et al. found that the ceramic $(Na_{0.5}Bi_{0.5})_{0.4}Sr_{0.6})$ $Ti_{0.99}Sn_{0.01}O_3$ had good energy-storage properties at room temperature, while its W_1 value decreased drastically to approximated 0.26 J/cm^3 under E = 50 kV/cm at 175 °C [6]. Verma et al. observed opposite variation for the ceramic $0.94Na_{0.5}Bi_{0.5}TiO_3$-$0.06KSbO_3$, which showed poor properties with $W_1 = 0.57$ J/cm^3 and $\eta = 53.2\%$ at room temperature and exhibited increased energy-storage behavior with

$W_1 = 0.73$ J/cm3 and $\eta = 72.3\%$ at 140 °C under E = 90 kV/cm [47]. The similar phenomenon was also reported for the ceramic $0.85(0.95BNT$-$0.05SrZrO_3)$-$0.15NaNbO_3$, which showed high W_1 of 3.14 J/cm^3 at 120 °C under high measurement electric field of 230 kV/cm [9]. In the present work, the ceramics BNBTA/0.06 exhibit medium energy-storage properties at room temperature. Furthermore, compared to the sample with $x = 0$, the change of W_1 and η of the sample BNBTA/0.06 is gentle with changing temperature. The sample with $x = 0.06$ exhibits better temperature stability over

Table 1 Comparison of energy-storage properties for BNBTA/x ceramics with other BNT-based ceramics

Compositions	W_1 (J/cm^3)	η (%)	E (kV/cm)	Temperature (°C)	References
BNBTA/0	0.28	5.4	70	R.T.	This work
BNBTA/0.04	0.64	42.3	70	R.T.	This work
BNBTA/0.06	0.82	67.7	70	R.T.	This work
BNBTA/0.08	0.71	69.3	70	R.T.	This work
BNBTA/0.06	0.78	71.3	50	R.T.	This work
BNBTA/0.06	0.76	84.5	50	180	This work
BNBTCZ	0.70	/	70	R.T.	[45]
BNBTCZ	~0.63*	/	60	~130*	[45]
BNKLSTT	2.24	64.3	130	R.T.	[46]
BNKLSTT	2.08	91.2	130	175	[46]
BNSTS	2.35	~65*	180	R.T.	[6]
BNSTS	~0.26*	~85*	50	175	[6]
BNTKS	0.57	53.2	90	R.T.	[47]
BNTKS	0.73	72.3	90	140	[47]
BNTSZNN	2.93	72	210	R.T.	[9]
BNTSZNN	3.14	79	230	120	[9]

The abbreviations are as following *Tem* measurement temperature, *R.T* room temperature, *BNBTCZ* 0.97BNBT-0.03CaZrO$_3$, *BNKL-STT* {{Bi$_{0.5}$[(Na$_{0.8}$K$_{0.2}$)$_{0.9}$Li$_{0.1}$]$_{0.5}$}}$_{0.96}$-Sr$_{0.04}$(Ti$_{0.975}$Ta$_{0.025}$)O$_3$, *BNSTS* (Na$_{0.5}$Bi$_{0.5}$)$_{0.4}$Sr$_{0.6}$)Ti$_{0.99}$Sn$_{0.01}$O$_3$, *BNTKS* 0.94Na$_{0.5}$Bi$_{0.5}$TiO$_3$-0.06KSbO$_3$, *BNTSZNN* 0.85(0.95BNT-0.05SrZrO$_3$)-0.15NaNbO$_3$

the test temperature range between room temperature and 180 °C. The results show that the doping of Al^{3+} facilitates improving temperature stability of ferroelectric properties and energy-storage performance.

4 Conclusions

The BNBTA/x ceramics with dense microstructure were successfully prepared via the solid-state reaction method. The ceramics with x ≤ 0.06 exhibit pure phase structure, while a second phase was found in the ceramic BNBTA/0.08. For the poled ceramics without Al^{3+} doping, three dielectric anomalies exist on the temperature-dependent dielectric spectra at the temperatures T_d, T_{RE}, and T_m. The Al^{3+}-doped ceramics only show two dielectric anomalies around T_{RE} and T_m, and the anomaly at T_d disappears. With the increase in the Al^{3+} amount, the temperature stability of dielectric constant between T_{RE} and T_m increases. The Al^{3+}-doping causes a decrease in ferroelectric properties. The P-E loops become slender with the increase in x, implying more pronounced relaxation behavior. The ceramic BNBTA/0.06 shows energy-storage density and energy-storage efficiency are 0.82 J/cm^3 and 67.7% under measurement electric field 70 kV/cm. As the temperature increases from 30 to 180 °C, the values of P_m, P_r and E_c for BNBTA/0.06 exhibits

gentle variation, and W_1 and η values change from 0.78 J/cm^3 and 71.3% to 0.76 J/cm^3 and 84.5% (under the measurement electric field E = 50 kV/cm), respectively. The results demonstrate that the doping of Al^{3+} facilitates improving temperature stability of both dielectric constant and energy-storage behavior.

References

1. Q. Xu, Y.H. Huang, M. Chen, W. Chen, B.H. Kim, B.K. Ahn, J. Phys. Chem. Solid. **69**, 1996 (2008)
2. S. Chaterjee, G. Agrawal, A. Mishra, S. Anwar, Mater. Today: Proceed. **5**, 24880 (2018)
3. X.S. Qiao, X.M. Chen, H.L. Lian, W.T. Chen, J.P. Zhou, P. Liu, J. Am. Ceram. Soc. **99**, 198 (2016)
4. X.S. Qiao, X.M. Chen, H.L. Lian, J.P. Zhou, P. Liu, J. Eur. Ceram. Soc. **36**, 3995 (2016)
5. G.H. Lee, Y.H. Kwon, J.H. Koh, Ceram. Int. **41**, 7897 (2015)
6. L.Y. Zhang, Z.Y. Wang, Y. Li, P. Chen, J. Cai, Y. Yan, Y.F. Zhou, D.W. Wang, G. Liu, J. Eur. Ceram. Soc. **39**, 3057 (2019)
7. J. Wang, X.M. Chen, X.M. Zhao, X.X. Liu, J.P. Zhou, P. Liu, Mater. Res. Bull. **67**, 94 (2015)
8. M. Shen, W.R. Li, M.Y. Li, H. Liu, J.M. Xu, S.Y. Qiu, G.Z. Zhang, Z.X. Lu, H.L. Li, S.L. Jiang, J. Eur. Ceram. Soc. **39**, 1810 (2019)
9. C.Q. Zhu, Z.M. Cai, B.C. Luo, L.M. Guo, L.T. Li, X.H. Wang, J. Mater. Chem. A **8**, 683 (2020)
10. K. McLaughlin, C. Pascual-Gonzalez, D. Wang, A. Feteira, J. Alloys Compd. **779**, 7 (2019)
11. T. Takenaka, K. Maruyama, K. Sakata, J. Appl. Phys. **30**, 2236 (1991)
12. F. Li, G.R. Chen, X. Liu, J.W. Zhai, B. Shen, S.D. Li, P. Li, K. Yang, H.R. Zeng, H.X. Yan, Appl. Phys. Lett. **110**, 182904 (2017)
13. L.N. Liu, X.M. Chen, R.Y. Jing, H.L. Lian, W.W. Wu, Y.P. Mou, P. Liu, J. Mater. Sci. - Mater. Electron. **30**, 5233 (2019)
14. R.Y. Jing, X.M. Chen, H.L. Lian, X.S. Qiao, X.J. Shao, J.P. Zhou, J. Eur. Ceram. Soc. **38**, 3111 (2018)
15. Q. Li, M.Y. Li, C. Wang, M.C. Zhang, H.Q. Fan, Ceram. Int. **45**, 19822 (2019)
16. Z. Fan, X. Tan, Script. Mater. **178**, 334 (2020)
17. L. Zhang, Z. Wang, Y. Li, P. Chen, J. Cai, Y. Yan, Y. Zhou, D. Wang, G. Liu, J. Eur. Ceram. Soc. **39**, 3057 (2019)
18. H.L. Lian, X.J. Shao, X.M. Chen, Ceram. Int. **44**, 11320 (2018)
19. H.L. Lian, X.J. Shao, R.X. Cheng, J. Mater. Sci. - Mater. Electron. **30**, 18539 (2019)
20. X.M. Chen, W.Y. Pan, H.H. Tian, X.X. Gong, X.B. Bian, P. Liu, J. Alloys Compd. **509**, 1824 (2011)
21. X.M. Chen, X.X. Gong, T.N. Li, Y. He, P. Liu, J. Alloys Compd. **507**, 535 (2010)
22. H.Y. Ma, X.M. Chen, J. Wang, K.T. Huo, H.L. Lian, P. Liu, Ceram. Int. **39**, 3721 (2013)
23. W.F. Bai, P. Li, L.Y. Li, J.J. Zhang, B. Shen, J.W. Zhai, J. Alloys Compd. **649**, 772 (2015)
24. P. Baettig, C.F. Schelle, R.L. Sar, U.V. Waghmare, N.A. Spaldin, Chem. Mater. **17**, 1376 (2005)
25. R. Ranjana, A.K. Kalyania, R. Garga, P.S.R. Krishna, Solid State Commun. **149**, 2098 (2009)
26. N. Vittayakorn, B. Boonchomd, J. Alloys Compd. **509**, 2304 (2011)
27. H.C. Yu, Z.G. Ye, J. Appl. Phys. **103**, 341141 (2008)
28. H.C. Yu, Z.G. Ye. J. Appl. Phys. Lett. **93**, 1129021 (2008)
29. A. Ullah, C.W. Ahn, A. Hussain, S.Y. Lee, W. Kim, J. Am. Ceram. Soc. **94**, 3915 (2011)

30. P. Fu, Z.J. Xu, R.Q. Chu, X.Y. Wu, W. Li, J. Alloys Compd. **535**, 5 (2012)
31. Y.Z. Qiu, X.M. Chen, H.L. Lian, J.P. Ma, W.Q. Ouyang, Mater. Chem. Phys. **202**, 197 (2017)
32. R.D. SHANNON, Acta Cryst. A **32**, 751 (1976)
33. Z.L. Yu, Y.F. Liu, M.Y. Shen, H. Qian, F.F. Li, Y.N. Lyu, Ceram. Int. **43**, 7653 (2017)
34. E.M. Anton, W. Jo, D. Damjanovic, J. Rödel, J. Appl. Phys. **110**, 094108 (2011)
35. E. Sapper, S. Schaab, W. Jo, T. Granzow, J. Rödel, J. Appl. Phys. **111**, 014105 (2012)
36. R.A. Malik, A. Hussain, A. Maqbool, A. Zaman, C.W. Ahn, J.U. Rahman, T.K. Song, W.J. Kim, M.H. Kim, J. Am. Ceram. Soc. **98**, 3842 (2015)
37. A.E. Glazounov, A.K. Tagantsev, A.J. Bell, Phys. Rev. B **53**, 11281 (1996)
38. M. Chen, Q. Xu, B.H. Kim, B.K. Ahn, J.H. Ko, W.J. Kang, O.J. Nam, J. Eur. Ceram. Soc. **28**, 843 (2008)
39. W. Jo, S. Schaab, E. Sapper, L.A. Schmitt, H.J. Kleebe, A.J. Bell, J. Rödel, J. Appl. Phys. **110**, 074106 (2011)
40. K. Uchino. S. Nomura, Ferroelectric. **44**, 55 (1982)
41. L. Jin, F. Li, S.J. Zhang, J. Am. Ceram. Soc. **97**, 1 (2014)
42. F. Li, R.Z. Zuo, D.G. Zheng, L. Li, J. Am. Ceram. Soc. **98**, 811 (2015)
43. H.B. Yang, F. Yan, Y. Lin, T. Wang, F. Wang, Sci. Rep. **7**, 8726 (2017)
44. H. Xie, Y.Y. Zhao, J.W. Xu, L. Yang, C.R. Zhou, H.B. Zhang, X.W. Zhang, W. Qiu, H. Wang, J. Alloys Compd. **743**, 73 (2018)
45. Q. Li, J. Wang, Y. Ma, L. Ma, G. Dong, H. Fan, J. Alloys Compd. **663**, 701 (2016)
46. J. Yin, Y. Zhang, X. Lv, J. Wu, J. Mater. Chem. A **6**, 9823 (2018)
47. A. Verma, A. Yadav, S. Kumar, V. Srihari, R. Jangir, H.K. Poswal, S. Biring, S. Sen, J. Mater. Sci.- Mater. Electron. **30**, 15005 (2019)